Ultrasonics 138 (2024) 107257

Contents lists available at ScienceDirect

Ultrasonics

journal homepage: www.elsevier.com/locate/ultras

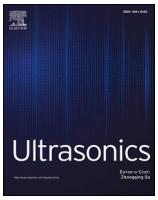

Can Mn:PIN-PMN-PT piezocrystal replace hard piezoceramic in power ultrasonic devices?

Xuan Li [a], Nicola Giuseppe Fenu [b], Nathan Giles-Donovan [c,d], Sandy Cochran [a], Margaret Lucas [a,*]

[a] Centre for Medical & Industrial Ultrasonics, James Watt School of Engineering, University of Glasgow, Glasgow G12 8QQ, UK
[b] Nami Surgical, 11 The Square, University Avenue, University of Glasgow, G12 8QQ, UK
[c] Department of Physics, University of California, Berkeley, CA 94720, USA
[d] Material Sciences Division, Lawrence Berkeley National Lab, Berkeley, CA 94720, USA

ARTICLE INFO

Keywords:
Power Ultrasonics
Bolted Langevin Transducer
Hard PZT
Mn:PIN-PMN-PT Piezocrystal
High-Power Impedance Spectroscopy

ABSTRACT

Mn:PIN-PMN-PT piezocrystal is investigated to determine whether its enhanced energy density makes it a candidate transducer material for power ultrasonics applications. To this end, the electromechanical and vibrational characteristics of a simple configuration of a bolted Langevin transducer (BLT) and then an ultrasonic surgical device, both incorporating Mn:PIN-PMN-PT piezocrystal, are compared with the same transducer configurations incorporating a conventional hard PZT piezoceramic commonly used in high-power ultrasonic transducers. The material properties of Mn:PIN-PMN-PT are determined using a single sample characterisation technique and these are used in finite element analysis (FEA) to design and then fabricate the BLT and ultrasonic surgical device, tuned to the first and second longitudinal modes at 20 kHz respectively. FEA is similarly used for the hard PZT versions. It is found that the superior elastic compliance of Mn:PIN-PMN-PT results in a higher radial piezo-stack deformation than the hard PZT under ultrasonic excitation of the BLT. However, the resulting longitudinal displacement amplitude of the two BLTs and two ultrasonic surgical devices is found to be equal, despite the higher figure of merit (Qk_{eff}^2) of those incorporating Mn:PIN-PMN-PT. The electrical impedance is measured at increasing excitation levels to evaluate the quality factor, Q. It is found that damping in the BLT with hard PZT is negligibly affected in the excitation range considered; however, the BLT incorporating Mn:PIN-PMN-PT exhibits a large reduction in Q. These findings indicate that, for measurements in air, the advantages of the high figure of merit of the piezocrystal material are not realised in a high-power transducer due to significantly increased damping at high excitation levels. To compare the vibrational response of the two ultrasonic surgical devices, L-C electrical impedance matching was implemented to maximise the efficiency of energy transfer from the source to the transducer under load. Results suggest that similar responses occurred for the two surgical devices in cutting tests using a low strength bone mimic material. However, the Mn:PIN-PMN-PT device exhibited better performance in cutting through higher strength *ex-vivo* chicken femur.

1. Introduction

M_n-doped $P_b(In_{1/2}Nb_{1/2})O_3$-$Pb(Mg_{1/3}Nb_{2/3})O_3$-$PbTiO_3$ (Mn:PIN-PMN-PT) single crystals are emerging as a potential material for use in high-power ultrasonics applications, due to their simultaneously high piezoelectric coefficient (d_{ij}), electromechanical coupling (k_{ij}), and mechanical quality factor (Q_m) [1,2,3]. When higher efficiency, lower electromechanical losses, and higher energy density are taken into account, these materials may allow realisation of more efficient transducers. As an example of the potential benefits, Mn:PIN-PMN-PT could be a candidate for miniaturising high-power ultrasonic devices that are based on BLTs so they can be readily integrated with robotics [4]. A potential application is minimally invasive ultrasonic surgical devices, especially because BLTs incorporating Mn:PIN-PMN-PT offer a more conventional device geometry than alternative approaches to miniaturisation, which have relied on, for example, flextensional [5] or planar [6] PZT transducer configurations to achieve a size reduction.

To contribute to understanding of the potential performance gain,

* Corresponding author.
E-mail address: Margaret.Lucas@glasgow.ac.uk (M. Lucas).

https://doi.org/10.1016/j.ultras.2024.107257
Received 13 November 2023; Received in revised form 24 January 2024; Accepted 27 January 2024
Available online 2 February 2024

the electromechanical and vibrational responses of two simple cylindrical half-wavelength 20 kHz bolted Langevin transducers (BLTs) and two ultrasonic surgical devices, tuned at their first and second longitudinal modes respectively, are compared: a half-wavelength transducer and a full-wavelength surgical device incorporating a hard PZT piezoceramic (PIC181, PI Ceramics, Germany) and a half-wavelength transducer and full-wavelength surgical device incorporating Mn:PIN-PMN-PT piezocrystal (TRS Technologies, USA).

Since Don Berlincourt, Bernard Jaffe, Hans Jaffe, Helmut Krueger and William Cook developed the lead zirconate titanate (PZT) materials in the Clevite Corporation, numerous differently-doped PZT compositions have emerged. Particularly, the family of piezoelectrically-hard PZTs (identified as PZT4, PZT8 etc.) has dominated high-power ultrasonics applications for over 60 years [7,8]. Recently, relaxor-PT piezoelectric single crystals, including doped ternary compositions such as Mn:PIN-PMN-PT, have started to capture the attention of transducer designers due to their simultaneously high electromechanical coupling ($k_{33} \sim 0.9$), mechanical quality factor ($Q_{33} \sim 1000$) and piezoelectric coefficients ($d_{33} > 2000$ pC/N). These extraordinary properties make them candidates for high-power applications. However, a drawback in their use is the relatively low temperature rhombohedral-to-tetragonal phase transition, T_{RT}, ([0 0 1] Poled $T_{RT} \sim 90 - 120°C$) when compared to PZT with Curie temperature, $T_C \sim 200 - 300$ °C. This limits the operating envelope of the material [1,2,3].

The higher electromechanical coupling factor, k_{ij}, of Mn:PIN-PMN-PT compared to hard PZT is indicative of its higher energy density. It links together the electromechanical coefficients and relates to the proportion of energy converted by the material as shown in Eq. (1) for $i,j = 3,3$ [9].

$$k_{33}^2 = \frac{d_{33}^2}{s_{33}^E.\varepsilon_{33}^T} = \frac{e_{33}^2}{c_{33}^E.\varepsilon_{33}^T} = \frac{e_{33}^2}{c_{33}^D.\varepsilon_{33}^S} \tag{1}$$

Referring to the constitutive equations [10], d_{33} and e_{33} are the piezoelectric coefficients in the strain-charge and stress-charge forms respectively; s_{33}^E and c_{33}^E are the elastic compliance and stiffness at constant electric field (superscript E) respectively; and ε_{33}^T and ε_{33}^S are the dielectric coefficients at constant stress (superscript T) and strain (superscript S) respectively.

k_{ij} is linked with the resonant vibrational mode geometries, specified by the subscripts, which obscure the inherent response of the material. By considering a generalized k, defined at zero frequency, the material's piezoelectric response may be decoupled from resonance phenomena, allowing an unbiased comparison [11]. Generally, the electromechanical coupling factor is defined as the ratio of converted energy to input energy and is described by Eq. (2) as follows,

$$k_G^2 = \sum_{i,j=1}^{6} \frac{d_{i3}c_{ij}^E d_{j3}}{\varepsilon_{33}^T} \tag{2}$$

which takes into account the absence of stress ($\nabla \cdot T = 0$ under static excitation) and assumes an electric field applied in the 3-direction. The inclusion of the summation fully incorporates the material anisotropy and quantifies all conversion mechanisms allowed by symmetry.

BLTs are ultrasonic vibration sources widely used for high-power ultrasonics applications and typically operate in resonance, tuned to a frequency in the range of 20 – 100 kHz [12,13,14]. The commonly adopted figures of merit (FoM) for BLTs are presented in Eq. (3) and Eq. (4). The mechanical quality factor (Q_{ij}) is directly proportional to the displacement achievable by the transducer at the resonance frequency and inversely proportional to transducer losses. Therefore, high Q_{ij}, high k_{ij}, which relates to transducer bandwidth and efficiency, and high piezoelectric coefficient d_{ij}, which relates to the output acoustic power, are all desired material characteristics for high power applications [1].

$$\text{FoM}_1 = k_{ij}^2.Q_{ij} \tag{3}$$

$$\text{FoM}_2 = d_{ij}.Q_{ij} \tag{4}$$

In addition, the acoustic power density, P_d, in Eq. (5), which approximates the maximum power that a transducer can deliver, and the vibration velocity, v_0, in Eq. (6) can also be used to estimate the piezoelectric material's performance [15].

$$P_d = 2\pi f_r E^2 k_{ij}^2 \varepsilon_{ij}^T Q_m \tag{5}$$

$$v_0 = \frac{4}{\pi}\sqrt{\frac{\varepsilon_{33}^T}{\rho}} k_{31} Q_m E \tag{6}$$

where E is the electric field, f_r represents the resonance frequency, and ρ is the density of the piezoelectric material.

2. Characterization of piezoelectric rings

Two piezoelectric rings, outer diameter 10 mm, inner diameter 5 mm and thickness 2 mm, were used to characterize both the PZT and Mn:PIN-PMN-PT materials. Electrical impedance measurements were taken using a calibrated custom fixture for an impedance analyser (Agilent 4294A, Keysight Technologies, USA) and curve fitting was carried out using the Piezoelectric Resonance Analysis Program (PRAP) (Tasi Technical Software, Canada). Finite element analysis (FEA) (Abaqus-Simulia, Dassault Systèmes, France) was used to simulate the two rings, with material properties provided by the manufacturer for the hard PZT (PIC181) and properties obtained through the single-sample characterization method [16,17] applied to a cube sample of [0 0 1]-poled Mn:PIN-PMN-PT.

As can be seen in Table 1, the hard PZT rings exhibit twice the value of Q_m, 80 % lower d_{33} and 30 % lower k_{33} than the Mn:PIN-PMN-PT

Table 1
Material properties of hard PZT and Mn:PIN-PMN-PT piezoelectric rings.

Parameter	Hard PZT	Mn:PIN-PMN-PT
Density ρ [kg/m^3]	7850	8130
Elastic stiffness coefficient c_{11}^E [N/m^2]	15.23×10^{10}	12.16×10^{10}
Elastic stiffness coefficient c_{12}^E [N/m^2]	8.91×10^{10}	10.49×10^{10}
Elastic stiffness coefficient c_{13}^E [N/m^2]	8.55×10^{10}	10.31×10^{10}
Elastic stiffness coefficient c_{33}^E [N/m^2]	13.41×10^{10}	11.10×10^{10}
Elastic stiffness coefficient c_{44}^E [N/m^2]	2.83×10^{10}	6.54×10^{10}
Elastic stiffness coefficient c_{66}^E [N/m^2]	3.16×10^{10}	6.21×10^{10}
Elastic compliance coefficient S_{11}^E [m^2/N]	1.175×10^{-11}	4.413×10^{-11}
Elastic compliance coefficient S_{12}^E [m^2/N]	-0.407×10^{-11}	-1.558×10^{-11}
Elastic compliance coefficient $S_{13}{}^E$ [m^2/N]	-0.499×10^{-11}	-2.652×10^{-11}
Elastic compliance coefficient $S_{33}{}^E$ [m^2/N]	1.411×10^{-11}	5.828×10^{-11}
Elastic compliance coefficient $S_{44}{}^E$ [m^2/N]	3.533×10^{-11}	1.531×10^{-11}
Elastic compliance coefficient $S_{66}{}^E$ [m^2/N]	3.164×10^{-11}	1.611×10^{-11}
Piezoelectric stress constant e_{33} [V • m/N]	14.70	15.32
Piezoelectric stress constant e_{31} [V • m/N]	−4.50	−5.15
Piezoelectric stress constant e_{15} [V • m/N]	11.00	8.19
Relative permittivity ε_{11}^S	740	1218
Relative permittivity ε_{11}^T	1224	1334
Relative permittivity ε_{33}^S	624	502
Relative permittivity ε_{33}^T	1135	3163
Piezoelectric charge coefficient d_{31} [pC/N]	−108	−553
Piezoelectric charge coefficient d_{33} [pC/N]	253	1166
Piezoelectric charge coefficient d_{15} [pC/N]	389	125
Coupling coefficient k_{33}	0.66	0.92
Coupling coefficient k_{31}	0.32	0.49
Coupling coefficient k_{15}	0.63	0.31
Coupling coefficient k_t	0.46	0.68
Coupling coefficient k_G	0.67	0.92
Mechanical quality factor Q_m	2200	1100
FoM$_1$	958	931
FoM$_2$ [pC/N]	557×10^3	1283×10^3
f_r [kHz]	20	20
E [V/m]	100	100
P_d[W/m^3]	12,102	32,766
v_0[m/s]	0.101	0.127

samples. Additionally, the hard PZT rings also exhibit 65 % lower ε_{33}^{T} and 75 % lower ${S_{11}}^{E}$ and ${S_{33}}^{E}$ compared to the Mn:PIN-PMN-PT samples, suggesting that the hard PZT material is much stiffer in both the radial and thickness directions. The calculated values for k_G using Eq. (2) are also included in Table 1, where the value for the Mn:PIN-PMN-PT material is 27 % higher than the hard PZT material. These results clearly show that the energy density, as quantified by k_G, is much higher for the Mn:PIN-PMN-PT than the hard PZT rings. The FoM values were also calculated for the two piezoelectric materials using Eqs. (3) and (4); both materials have similar FoM_1 due to the higher Q_m and lower k_{33} for the hard PZT material, and lower Q_m and higher k_{33} for the Mn:PIN-PMN-PT material. However, FoM_2 for the Mn:PIN-PMN-PT material is 57 % higher than the hard PZT material, suggesting that this material will develop higher vibration velocity in the thickness direction at resonance [18]. The acoustic power density, P_d, and vibration velocity, v_0, for 20 kHz BLTs made with the two different piezoelectric materials were estimated from Eqs. (5) and (6) for electrical field strength $E = 100$ V/m. The results in Table 1 again highlight potential benefits of Mn:PIN-PMN-PT, showing that the BLT incorporating the piezocrystal rings has 63 % higher calculated power density and 25 % higher longitudinal vibration velocity than the BLT incorporating hard PZT. Despite the extraordinary properties of Mn:PIN-PMn-PT rings, the variation in the piezoelectric material properties can be significant. It was reported in [4] that the four Mn:PIN-PMN-PT rings present non-negligible differences. However, the consistency of the properties of the pairs of Mn:PIN-PMN-PT and hard PZT rings has been confirmed in this study.

Fig. 1 presents a comparison between the measured electrical impedance magnitude and phase of the piezoelectric rings from 10 kHz to 1 MHz. The hard PZT ring shows three major peaks, denoted as modes I, II and III, whereas the Mn:PIN-PMN-PT ring presents a significantly higher modal density, with more than ten clear peaks within the same frequency range. The first eight peaks, all with relatively low impedance magnitude and therefore easier excitation, were analyzed.

To identify the vibration mode shapes, FEA simulation of rings of both materials was performed and compared with experimental modal analysis results obtained with a 3D laser Doppler vibrometer (LDV) (MSA 100, Polytec, Germany). The results are presented in Figs. 2, 3 and 4. From the frequency response characteristics of the surface vibration velocities of the piezoelectric rings, shown in Fig. 2, it can be observed that the Mn:PIN-PMN-PT ring developed considerably higher velocity magnitudes in most of its modes than the hard PZT ring, for the same 1 $V_{0\text{-}p}$ excitation amplitude, giving a first indication that this material might be capable of generating larger displacement amplitudes when incorporated in a BLT.

For the hard PZT ring (Fig. 3) mode I is the classic 3rd radial mode of a ring or cylinder, characterized by 6 radial nodal lines on the ring surface or 6 nodal planar surfaces created by extending those nodal lines axially along the outer and inner circumferences of the cylinder. This is supported by the mode I measurement in Fig. 2(a), that exhibits equal vibration amplitude in the x- and y-directions, much larger than in the z-direction, and the LDV measurement that shows a close match (difference < 0.5 %) between predicted and measured f_r. Mode II is identified as the thickness mode of the ring, equivalent to the 1st axial mode of a cylinder; the motion in the z-direction of the ring is clearly more prominent in Fig. 2(a). The mode shape is further characterized for this material by the mean circumference of the ring (between the outer and inner circumferences) moving with significantly higher amplitude than the inner and outer circumferences themselves, as is clear in Fig. 3. There is again close match (difference < 0.7 %) between the predicted and measured values of f_r. Fig. 2(a) shows that mode III exhibits very similar x, y, and z components of ring motion amplitude and, in Fig. 3, it is observed that this mode primarily exhibits bending of its cross-section, where the inner and outer circumferences move in phase while the mean circumference moves in anti-phase, with an additional continuous variation in the bending amplitude on the anti-nodal inner and outer circumferences. With this much more complex mode shape, the match for f_r is poorer at 3.3 %.

In contrast, all the Mn:PIN-PMN-PT ring modes shown in Fig. 4, measured within the same frequency range, are much more complex, even at the lower frequencies. For example, mode I is a radial mode,

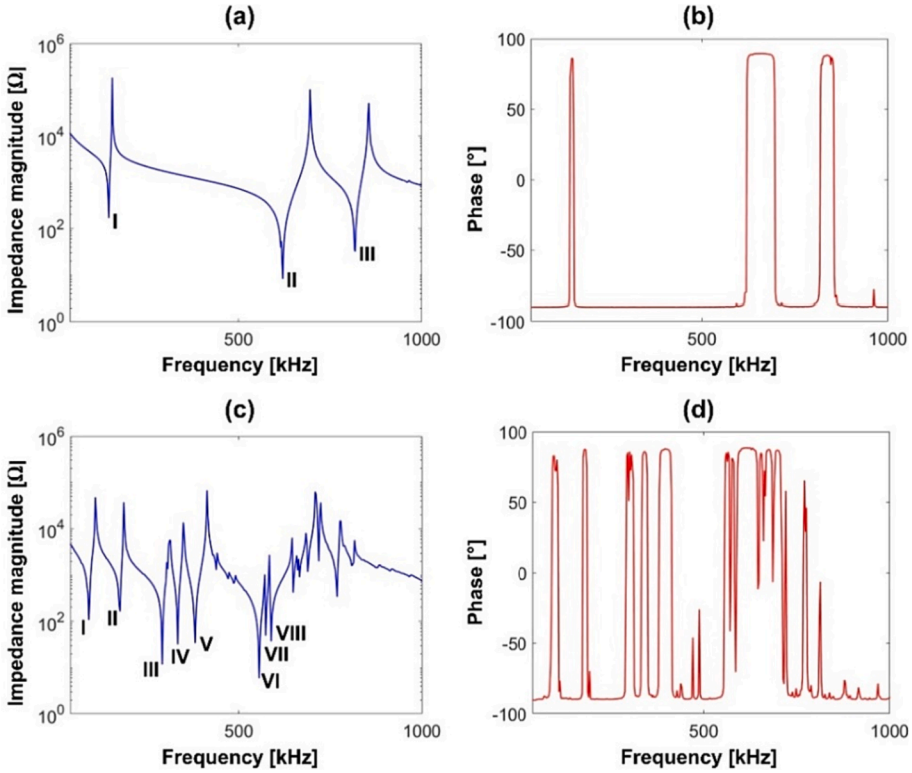

Fig. 1. Impedance magnitude and phase characteristics of (a) and (b) hard PZT, and (c) and (d) Mn:PIN-PMN-PT rings.

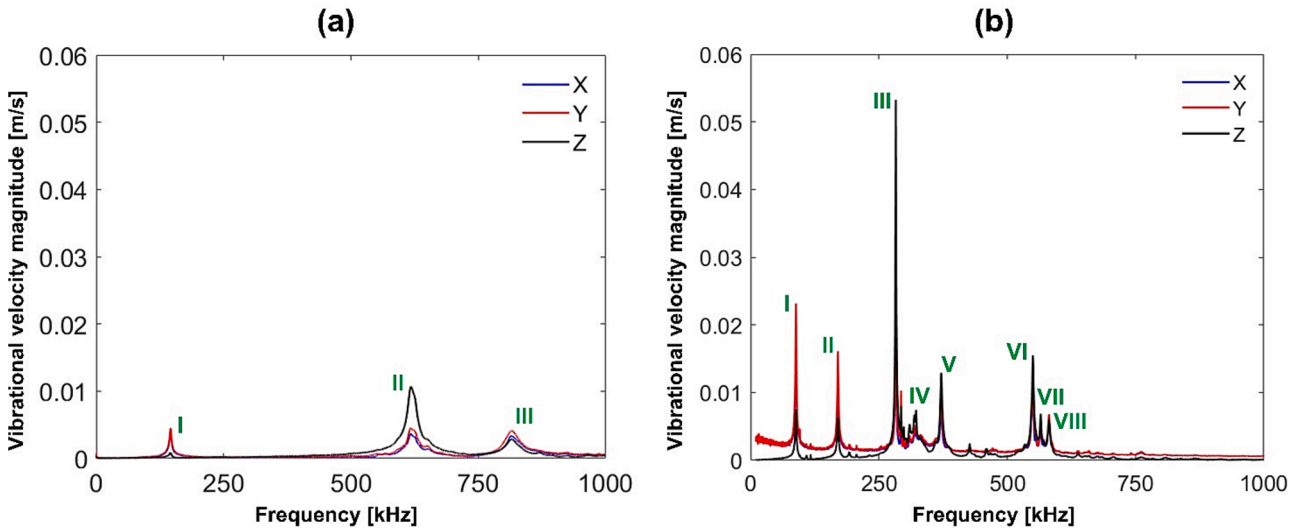

Fig. 2. Frequency response of the surface vibration velocity of the piezoelectric rings with 1 $V_{0\text{-}p}$ excitation for (a) hard PZT ring, (b) Mn:PIN-PMN-PT ring.

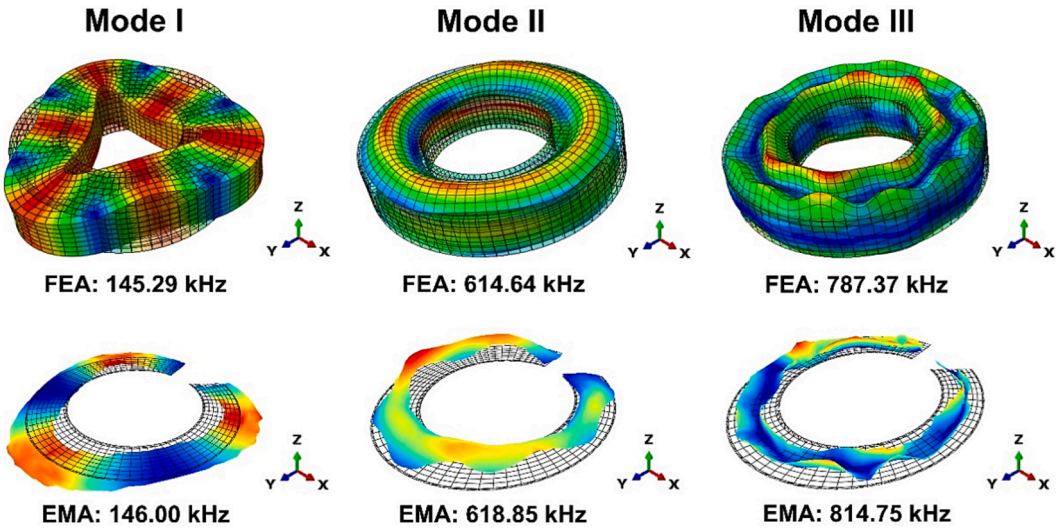

Fig. 3. Comparison between mode shapes obtained from FEA (full 3D model) and 3D LDV measurements from one surface at f_r for the hard PZT ring. (Note there is no LDV measurement data for the area covering the electrode/wire connection). Warm (red) to cool (blue) colours indicate anti-nodes to nodes respectively. (For interpretation of the references to colour in this figure legend, the reader is referred to the web version of this article.)

commonly referred to as the 'breathing' mode or R0 of a ring, but it does not exhibit the radial uniformity of a conventional R0 mode, additionally exhibiting circumferential motion consistent with an R4 mode evident as four full circumferential wavelengths. The pure R4 mode is mode II. Mode III is the dominant mode seen in the frequency response in Fig. 2(b), with its own response dominated by motion in the axial (z-) direction. Mode III is a thickness mode but, again, there is an additional surface axial nonuniformity that is characterised by four wavelengths around the circumference (Fig. 4). These four wavelength axial motions are also seen in modes IV and V. Although no pure thickness mode is identified, if it is assumed that mode III is the equivalent for a ring of this material, then the resonance frequency is much lower than the thickness mode frequency for the PZT ring, which is consistent with the much higher elastic compliance of Mn:PIN-PMN-PT. For the modes in Fig. 4, the differences between the FEA and measured values of f_r are often larger than for the PZT ring, however, the match is extremely close for some modes, e.g. 0.3 % for mode VI, and within 5 % for modes I to III.

Compared to hard PZT, the material properties of Mn:PIN-PMN-PT are not as well-documented and there is less well-established properties data. Also, the variation in properties between samples of Mn:PIN-PMN-PT is much higher and less well controlled than PZT. These issues result in the mismatch in resonance frequencies being generally larger than for the hard PZT ring. The Mn:PIN-PMN-PT ring also presents a much higher modal density and more complex mode shapes than the hard PZT ring, so the locations where the electric wires are attached to the surface electrode of the ring (for the experimental modal analysis) are more likely to be close to high deformation regions where small additional mass and/or stiffness affect the resonance frequencies.

3. Comparison of BLTs and cutting devices incorporating hard PZT and Mn:PIN-PMN-PT rings

3.1. The ultrasonic devices

Fig. 5 shows a simple configuration of an ultrasonic surgical device which incorporates a pair of rings of hard PZT or Mn:PIN-PMN-PT. The device comprises two parts: a half wavelength BLT and a half wavelength stepped horn with a thin (0.5 mm thickness) and round (4 mm in diameter) blade. The BLT is tuned to its first longitudinal mode, L1, close to 20 kHz. The horn-blade part can be connected using a threaded stud

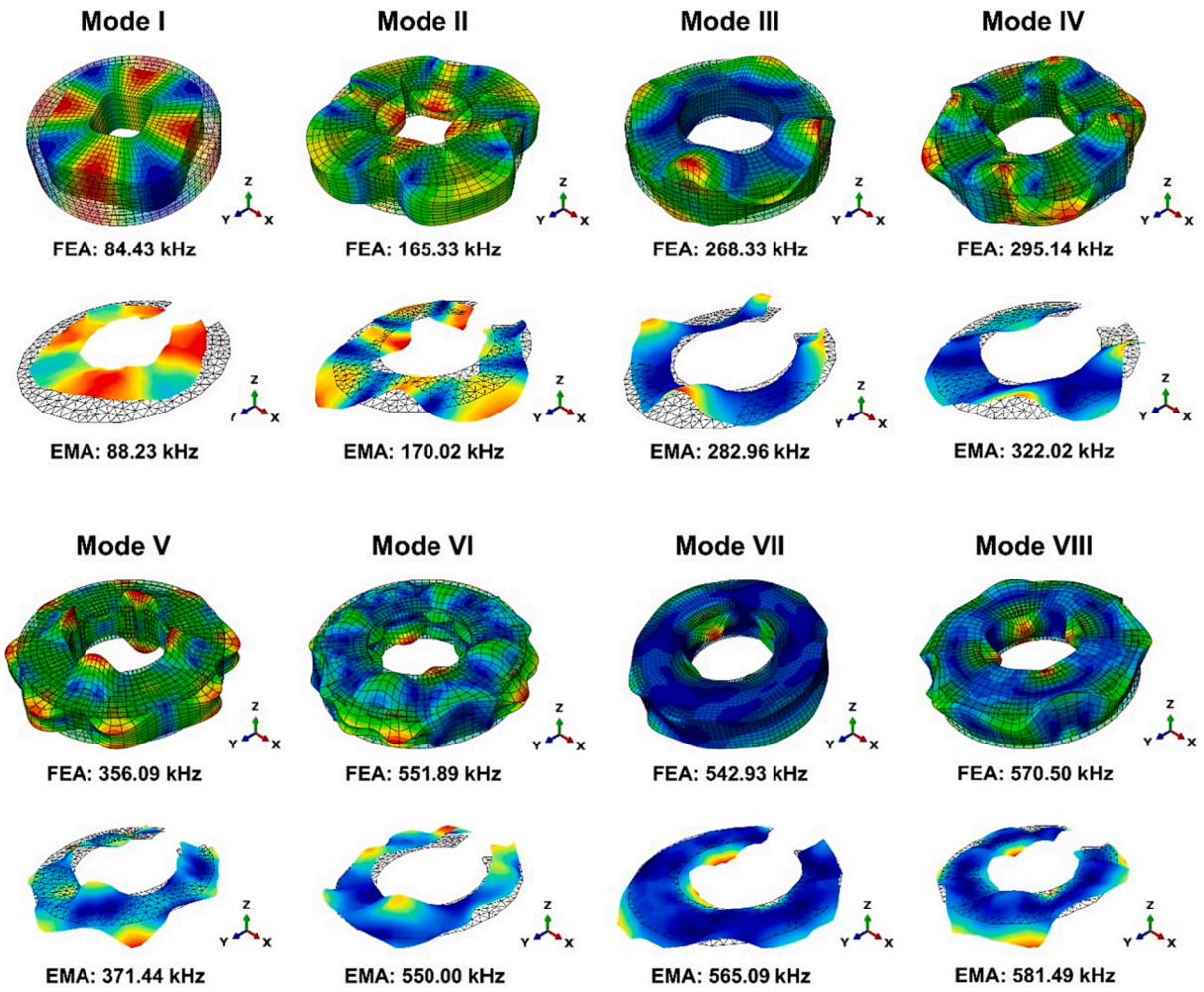

Fig. 4. Comparison between mode shapes obtained from FEA (full 3D model) and 3D LDV measurements from one surface at f_r for Mn:PIN-PMN-PT ring. (Note there is no LDV measurement data for the area covering the electrode/wire connection). Warm (red) to cool (blue) colour indicates anti-nodes to nodes respectively. (For interpretation of the references to colour in this figure legend, the reader is referred to the web version of this article.)

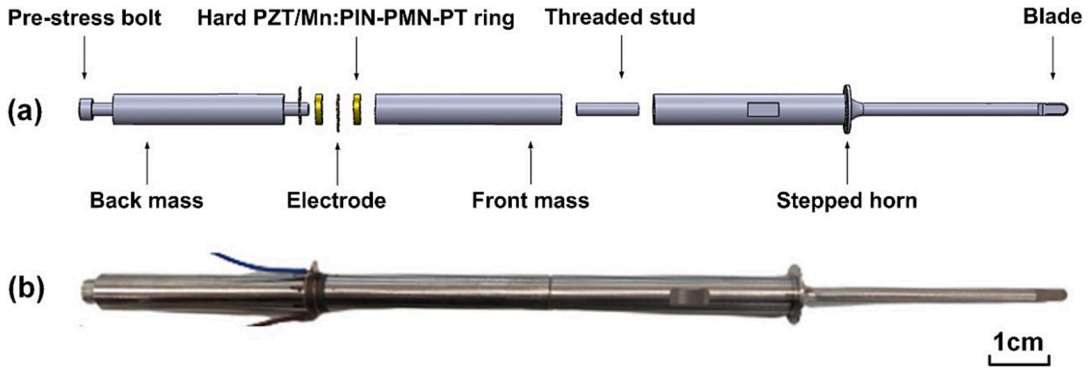

Fig. 5. (a) Exploded view of a full wavelength 20 kHz ultrasonic surgical device. (b) Image of one of the fabricated surgical devices.

to form a full wavelength, L2-mode, 20 kHz ultrasonic surgical tool. There is a small flange located at the step in the horn, at the displacement node, allowing the device to be attached to a casing for tissue cutting experiments. The front mass, back mass, threaded stud and stepped horn are all made from titanium grade 5 alloy Ti6Al4V, the pre-stress bolt is A4 tool steel, and the electrode material is copper [19].

Pre-stress was applied to the piezoelectric rings in the BLT following guidelines for achieving a stable impedance response of the transducer without risking depolarisation [20,21]. For the hard PZT BLT, with a recommended pre-stress in the region of 30 MPa [22], the applied torque was 3.0 Nm. However, for the Mn:PIN-PMN-PT BLT there is no reported recommendation for the pre-stress. Since it is known that the material is more fragile, the applied torque was increased slowly, in small increments, until it was evident that electrical stability was reached by monitoring the impedance, ultimately with an applied torque of 2.5 Nm.

3.2. Characterisations

All the fabricated devices were characterised using electrical impedance analysis (IA), experimental modal analysis (EMA) and harmonic response analysis (HA) to compare their ability to achieve large displacement amplitudes. The influence of high excitation level on the electromechanical characteristics (electrical impedance, coupling coefficient, mechanical quality factor and ultrasonic power) were additionally investigated and compared for the two BLTs.

3.2.1. Electrical impedance analysis

Electrical impedance measurements of the BLTs excited in their L1 mode and of the surgical devices in their L2 mode are shown in Fig. 6. The effective electromechanical coupling coefficient, k_{eff}, was calculated (Table 2) using Eq. (7) [23], where f_a is the anti-resonance frequency.

$$k_{\text{eff}}^2 = \frac{f_a^2 - f_r^2}{f_a^2} \tag{7}$$

The effective mechanical quality factor was calculated from Eq. (8), where f_1 and f_2 are frequencies either side of f_r corresponding to an impedance magnitude 3 dB higher than the impedance magnitude measured at f_r.

$$Q = \frac{f_r}{f_1 - f_2} \tag{8}$$

From Fig. 6, the Mn:PIN-PMN-PT BLT and surgical device exhibit larger bandwidth (difference between f_a and f_r), hence higher k_{eff} and the impedance is much lower. The electrical characteristics of all devices are summarised in Table 2.

The hard PZT half wavelength BLT has > 50 % lower k_{eff} but 44 % higher Q than the Mn:PIN-PMN-PT BLT, resulting in a 60 % lower FoM_1. Furthermore, the Mn:PIN-PMN-PT BLT has > 80 % lower impedance magnitude than the hard PZT BLT, due to the considerably larger value of d_{33} for the piezocrystal material (see Table 1). For the full wavelength ultrasonic surgical devices, the hard PZT device similarly has > 50 % lower k_{eff} than the Mn:PIN-PMN-PT device; however, the values of Q are within 10 % of each other. As a result, FoM_1 for the Mn:PIN-PMN-PT device is four times higher than for the hard PZT device. Additionally, its impedance magnitude is almost nine times lower. Therefore, it could be expected that the combination of higher FoM_1, lower impedance magnitude and similar Q, is an indication that Mn:PIN-PMN-PT is a suitable candidate material for an ultrasonic surgical device.

From Table 2 it is also observed that, when the stepped horn and blade are attached to the BLT, the impedance magnitude approximately doubles, k_{eff} approximately halves, and Q approximately doubles, and this is consistent for both surgical devices. Similar findings have been reported previously [13,14,24]; as the volume of piezoelectric material decreases as a proportion of the device volume, the coupling coefficient decreases and the impedance magnitude and Q increase. This

Table 2
Characteristics of the BLTs and ultrasonic surgical devices from impedance measurements.

	f_r [kHz]	Z [Ω]	k_{eff}	Q	Qk_{eff}^2 (FoM_1)
Hard PZT BLT	20.45	433	0.154	794	18.8
Mn:PIN-PMN-PT BLT	21.03	80	0.319	447	45.5
Hard PZT surgical device	20.45	1290	0.068	1257	5.8
Mn:PIN-PMN-PT surgical device	20.69	148	0.142	1113	22.4

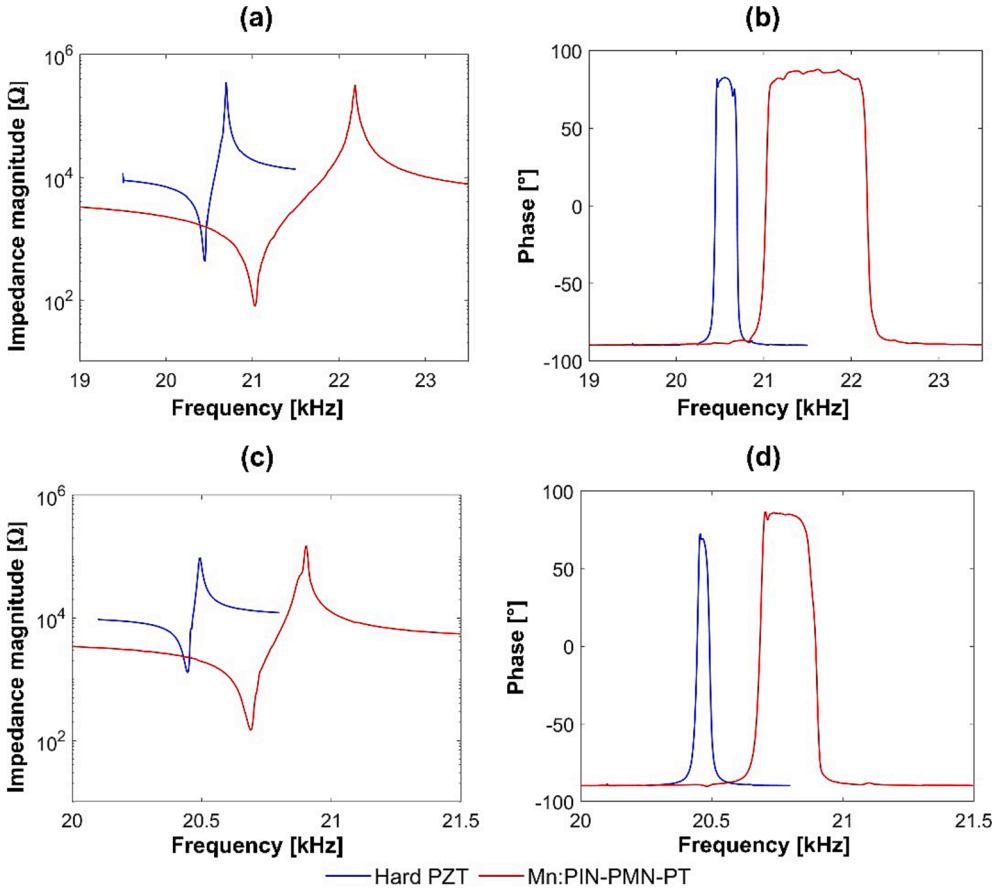

Fig. 6. Measured electrical impedance of hard PZT and Mn:PIN-PMN-PT devices: BLTs impedance (a) magnitude and (b) phase; surgical devices impedance (c) magnitude and (d) phase.

consistency between devices made with the two different materials is another promising indicator of the potential use of Mn:PIN-PMN-PT in devices based on the Langevin transducer structure.

3.2.2. Experimental modal analysis

Experimental modal analysis was performed using a 3D LDV (CLV3000, Polytec, Germany). Frequency response functions (FRFs) were acquired from a grid of measurement points on the device surface, from which the modal parameters (f_r, damping, and mode shape) were extracted. A white noise excitation signal of 15 V_{rms} was generated by a signal generator (Quattro, Data Physics, UK) and amplified by a power amplifier (RMX 4050HD, QSC, USA) before being supplied to the transducers. The LDV measured three orthogonal components of the vibrational velocity from each grid point. Data acquisition and processing software (SignalCalc, Data Physics, UK) was used to calculate the FRFs from the excitation and response signals and then to apply a curve-fitting routine to extract the FRF magnitude and phase data. Finally, the measured FRFs were exported into modal analysis software (ME'scopeVES, Vibrant Technology, USA) to extract the modal parameters.

Fig. 7 shows the tuned longitudinal mode shapes (as colour contours and waveforms) of the BLTs and ultrasonic surgical devices, as predicted by FEA and measured by EMA. The predicted and measured modes are in close agreement with respect to the location of the nodal planes (nodes are at the piezoelectric ring stack and step of the horn where the flange is located) and gain values, defined as the vibration amplitude ratio between the two ends of the BLT, or between the tip of the surgical device and end of its back mass; these are approximately 1.2 and 7 respectively.

Much higher deformation of the Mn:PIN-PMN-PT rings in the BLT can be seen in the FEA results which is due to the higher elastic compliances than for the hard PZT material (see Table 1). Values of Q were calculated for the BLTs from the modal damping and found to be 903 and 735 for the hard PZT and Mn:PIN-PMN-PT BLTs, respectively, and 1714 and 1205, respectively, for the surgical devices. These are much higher than the values of Q calculated from the impedance measurements, Table 2. This highlights that damping is excitation level dependent and that realistic comparisons of Q need to be made at excitation levels typical of device operation, with the comparison also affected by the loading condition.

3.2.3. Piezoelectric stack deformation

Due to the observation of higher deformation of the Mn:PIN-PMN-PT stack in the mode shapes in Fig. 7, which suggests that this material develops higher axial and radial displacements, more detailed EMA was conducted on the piezoelectric stack of both BLTs.

Fig. 8(a) illustrates the 32-point measurement grid applied to each piezoelectric stack. Each circumference (c.1, c.2, c.3, and c.4) divides the piezoelectric stack into eight quadrants. For each ring, there are two equally spaced points in its thickness direction. Fig. 8(b) presents the normalised piezoelectric stack radial deformations averaged for all measurement points, compared with the similarly normalized FEA results.

The Mn:PIN-PMN-PT stack exhibits much higher deformation (average is 70 % higher from FEA and 80 % higher from EMA). Both stacks exhibit radial deformation nonuniformity, as seen in the FEA images in Fig. 8(b), the nonuniformity being larger (using the same scaling) for the Mn:PIN-PMN-PT stack. These results are consistent with the higher elastic compliance of the Mn:PIN-PMN-PT material in both thickness and radial directions (see Table 1).

3.2.4. Harmonic analysis

To study the vibration responses of the devices at increasing excitation levels, harmonic analysis was performed. A desktop PC running bespoke software coded with LabVIEW (NI, USA) controls the signal generator (33210A, Keysight Technologies, USA) input to a power amplifier (HFVA-62, Nanjing Foneng Technology Industry, China). Built-in probes in the power amplifier allow current and voltage to be measured with a 500 kHz DAQ card (USB-6346, NI, USA). A 1D LDV (OFV 303, Polytec, Germany) measures the normal-to-surface vibration velocity of the radiating face of the devices, which is then converted to displacement. The piezoelectric stack was excited at increasing increments of voltage in a frequency sweep incremented from just below to just above the resonance frequency, using gated sine signals. A 3-second time gap between successive frequency increments was implemented to ensure dissipation of heat between measurements, avoiding any thermal contribution to the vibrational response. The results for the two BLTs and two ultrasonic surgical devices are shown in Fig. 9.

Typical of slender BLTs, and BLTs connected to slender tips, nonlinear softening responses are observed, with the backbone of the

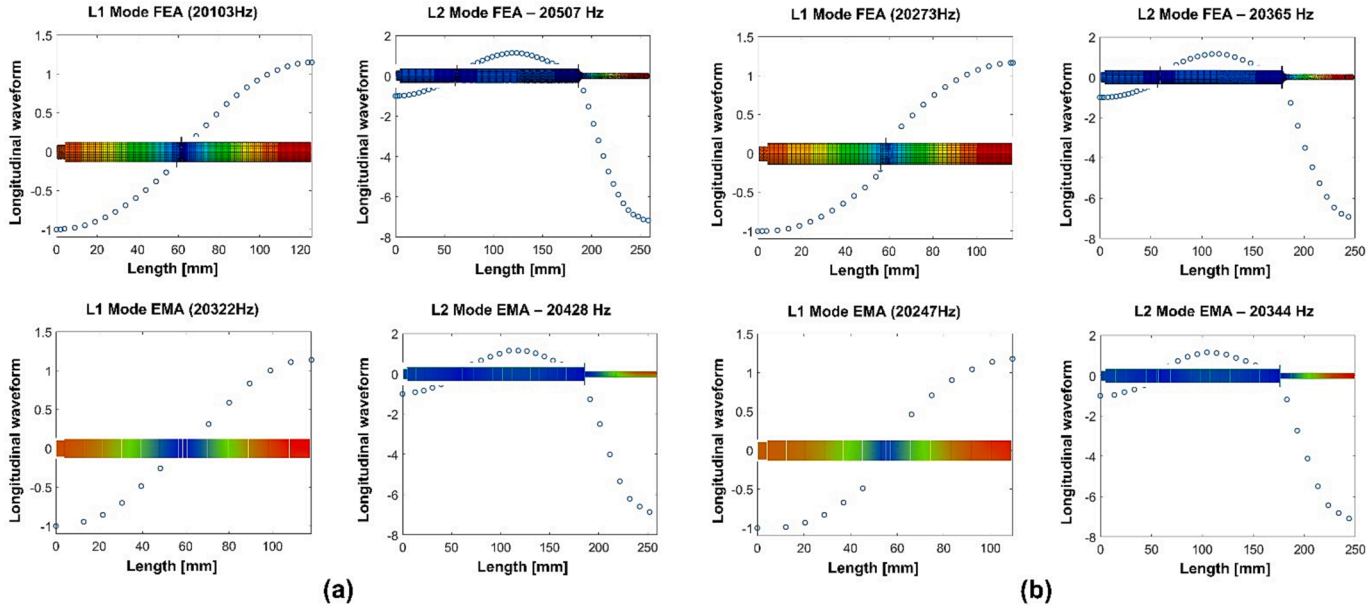

Fig. 7. Comparison of mode shapes between FEA and EMA of BLTs and ultrasonic surgical devices with (a) hard PZT and (b) Mn:PIN-PMN-PT rings. Warm (red) to cool (blue) colour indicates anti-nodes to nodes respectively. (For interpretation of the references to colour in this figure legend, the reader is referred to the web version of this article.)

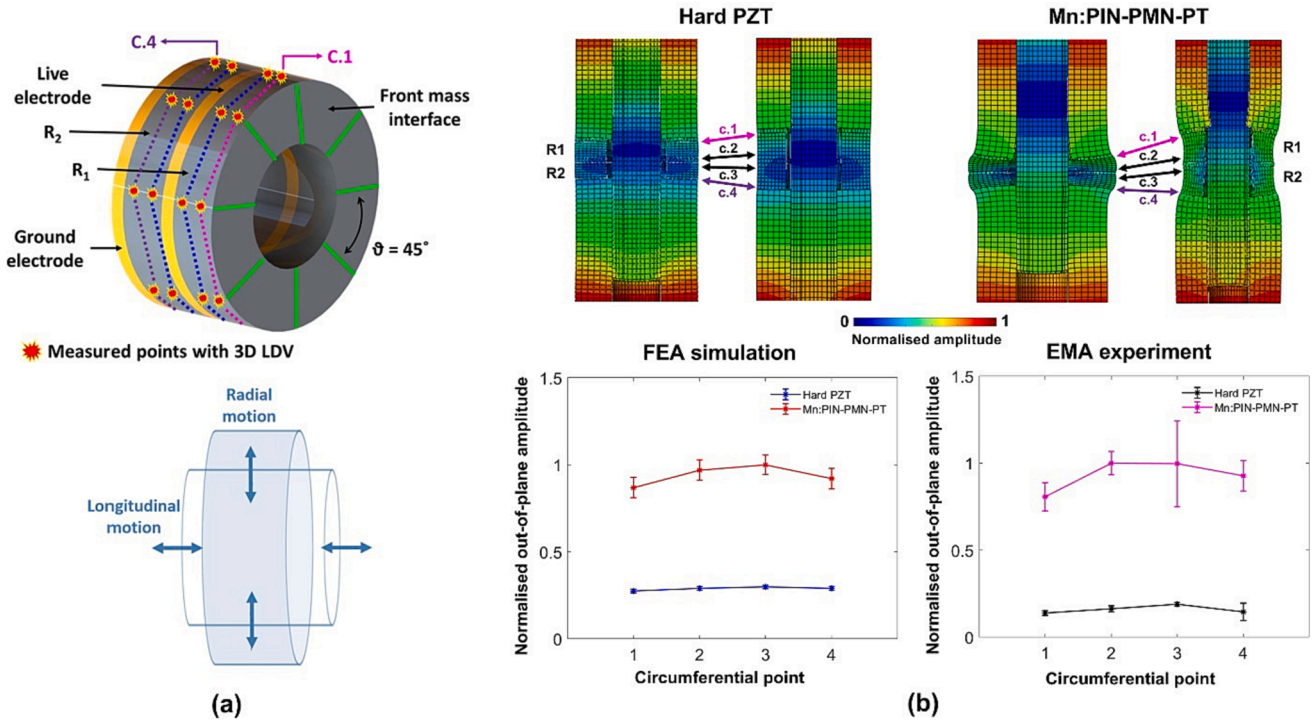

Fig. 8. (a) The LDV measurement grid on the piezoelectric stack. (b) Normalised FEA and EMA radial stack deformations of the BLTs in their L1 mode.

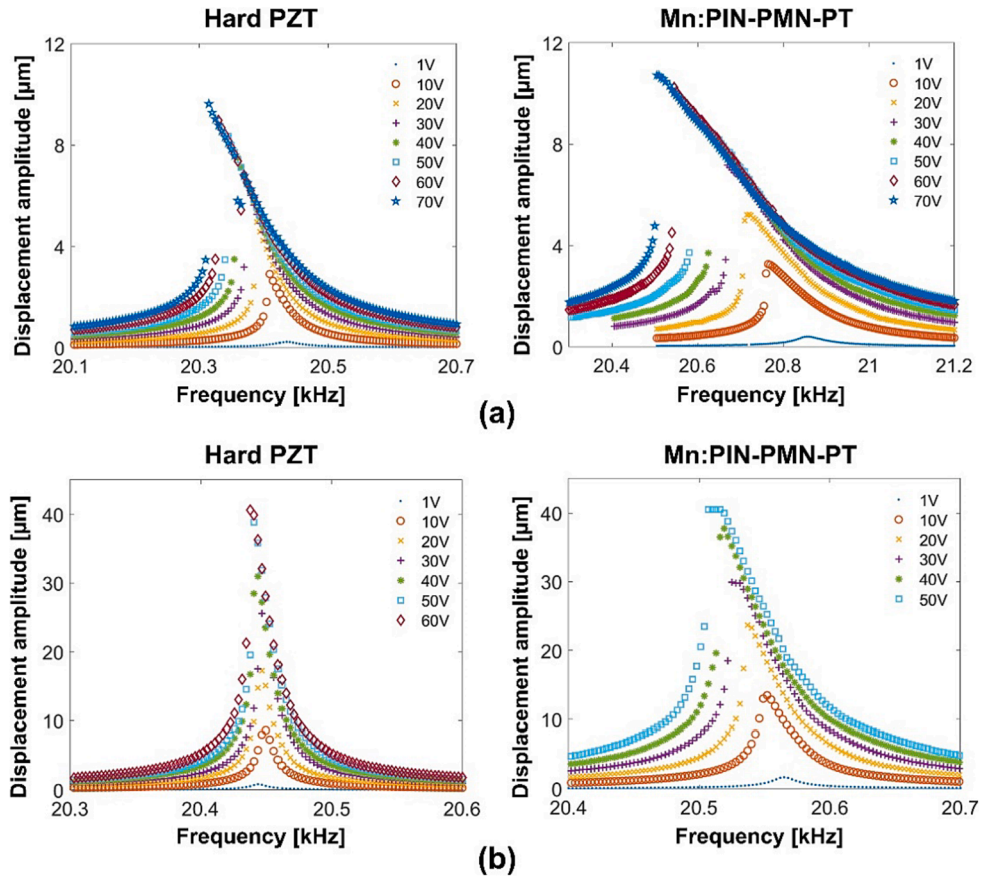

Fig. 9. Vibration response at increasing excitation levels of hard PZT and Mn:PIN-PMN-PT (a) BLTs and (b) ultrasonic surgical devices.

response curve bending to the left as excitation level increases [12]; nonlinearity is stronger for the Mn:PIN-PMN-PT BLT and surgical device. The nonlinear response is an indicator of performance and efficiency of the piezoelectric material [25,26,27,28,29]. In this case, the results show that the piezoelectric properties of Mn:PIN-PMN-PT are more dependent on excitation level than the properties of hard PZT when incorporated in a BLT or surgical device, indicating the potential for a less stable vibrational response at operating excitation levels. However, the two BLTs and two surgical devices achieve very similar displacement amplitudes at resonance, with the Mn:PIN-PMN-PT BLT being slightly higher (11 μm at 70 V_{rms}) than for the hard PZT (10 μm at 70 V_{rms}), and the surgical devices both delivering 41 μm displacements at 50 V_{rms}.

3.2.5. Electrical characteristics, relationship with excitation voltage

Electrical impedance is normally measured with 1 $V_{P\text{-}P}$ applied across the piezoelectric stack, under the assumption that the transducer's vibrational response is linear. However, it is known that f_r usually decreases with increasing excitation level. This behaviour is known as 'softening', and it encompasses the known and inseparable non-linear effects of mechanical loss, self-heating and vibrational stress, as well as the non-linear relationships between piezoelectric properties and excitation level, all of which affect the dynamic response of the devices. To investigate this effect further, the excitation current and voltage magnitudes were used to calculate the electrical impedance at incremented excitation levels. Meanwhile, f_r and f_a were acquired from the impedance–frequency measurements to calculate the coupling coefficient, k_{eff}, from Eq. (7) at different excitation levels. Additionally, the power density, P_d, for both BLTs was calculated using Eq. (9),

$$P_d = \frac{UI\cos\theta}{V} \tag{9}$$

where U and I are the amplitudes of voltage and current respectively, θ represents the phase difference between voltage and current and V is the volume of piezoelectric material in a pair of rings.

The results in Fig. 10 show that, within the excitation range of the experiment, the impedance magnitude of both BLTs increases with applied voltage with a nearly linear relationship; for the hard PZT BLT the impedance magnitude increased by 43 %, with a slope of 4.2 Ω/V, and for the Mn:PIN-PMN-PT BLT the impedance magnitude increased by 300 %, with a slope of 1.9 Ω/V. The coupling coefficient, k_{eff}, on the other hand stays almost constant, the slight linear increase being mainly associated with the decreasing f_r shown in Fig. 9. The power density, P_d, of the Mn:PIN-PMN-PT and PZT BLTs is similar at low excitation voltage levels but the Mn:PIN-PMN-PT BLT exhibits much higher P_d as applied voltage increases, indicating that it has much better load handling capacity than the hard PZT BLT. However, this could be unachievable in practice due to the comparatively high measured deformation of the Mn:PIN-PMN-PT rings in the transverse direction.

3.2.6. Mechanical Q factor relationship with excitation voltage

Conventionally, Q is determined using the 3 dB method (Table 2) from a 1 $V_{p\text{-}p}$ excitation of the BLT using impedance analysis (IA). Alternatively, Q can be estimated in the tuned mode from EMA modal data; although the excitation level is higher than for IA, it is still assumed that losses are excitation level independent. It is therefore of interest to study how the mechanical Q factor of the BLTs is affected by excitation level.

In a standard method to measure the mechanical Q of a transducer at high excitation levels [30], the transducer is excited by a burst voltage signal at its resonance frequency. The duration of the burst needs to be sufficiently long to allow the transducer to reach steady state but short enough to prevent self-heating. Immediately after the burst, the transducer terminals are short circuited by the power amplifier so that the current, I, and hence vibration velocity, decay exponentially with time as expressed in Eq. (10), where α represents the steady state current amplitude, φ takes into account any possible offset (bias) in the signal, t is time, and γ is the exponential coefficient.

$$I = \alpha e^{-\gamma t} + \varphi \tag{10}$$

If γ is calculated from the signal decay of I or the velocity in the time domain then Q can be estimated from Eq. (11).

$$Q = \pi \frac{f_r}{\gamma} \tag{11}$$

Fig. 11(a) shows the results of voltage, current and velocity time traces with a 500 kHz sampling frequency to capture the full decay profile in the transient response. The coefficients α, γ, and φ were estimated from a fit of Eq. (11) to the decay envelopes of both current and velocity, with a 95 % confidence bound. These bounds were used to estimate the error in Q using standard error propagation techniques, such as in Eq. (12),

$$\Delta Q = \frac{\pi f_r}{\gamma^2} \Delta\gamma \tag{12}$$

where ΔQ and $\Delta\gamma$ are the error in Q and γ respectively. Fig. 11(b) shows the results of the application of the transient method on both current and velocity to measure Q of both BLTs in the L1 mode, with the burst signal voltage incremented from 1 to 70 V_{rms}. Error bars are included; however the error calculated from Eq. (12) is very small, thus confirming the accuracy of the method.

For the hard PZT BLT, Q fluctuates with a maximum variation of 14 % and exhibits a value in excess of 600. In comparison, Q for the Mn:PIN-PMN-PT BLT is significantly affected by excitation level, decreasing from 320 to 100, an almost 70 % reduction. This indicates that damping

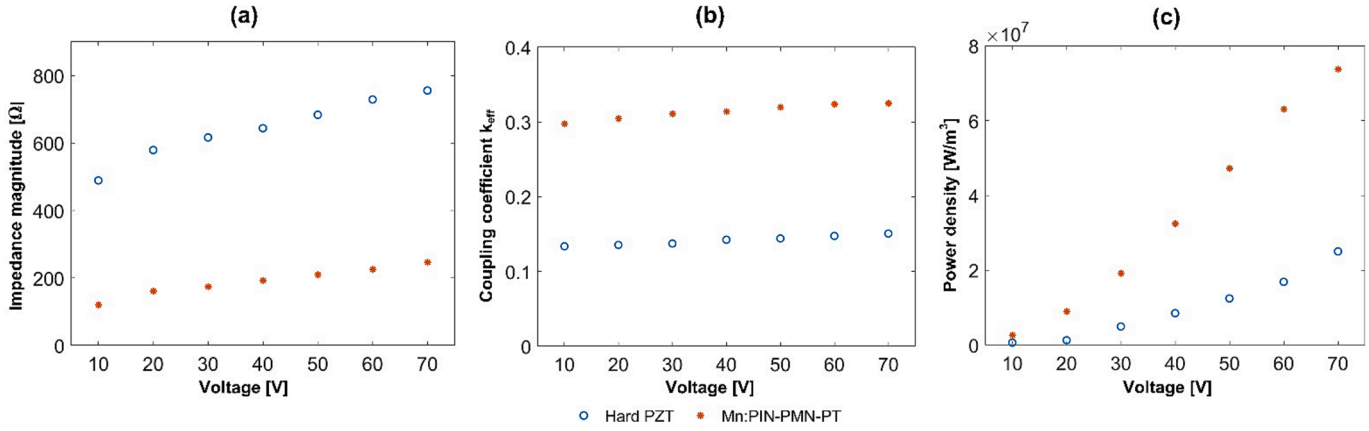

Fig. 10. (a) Impedance magnitude, (b) coupling coefficient and (c) power density as a function of excitation voltage for the BLTs.

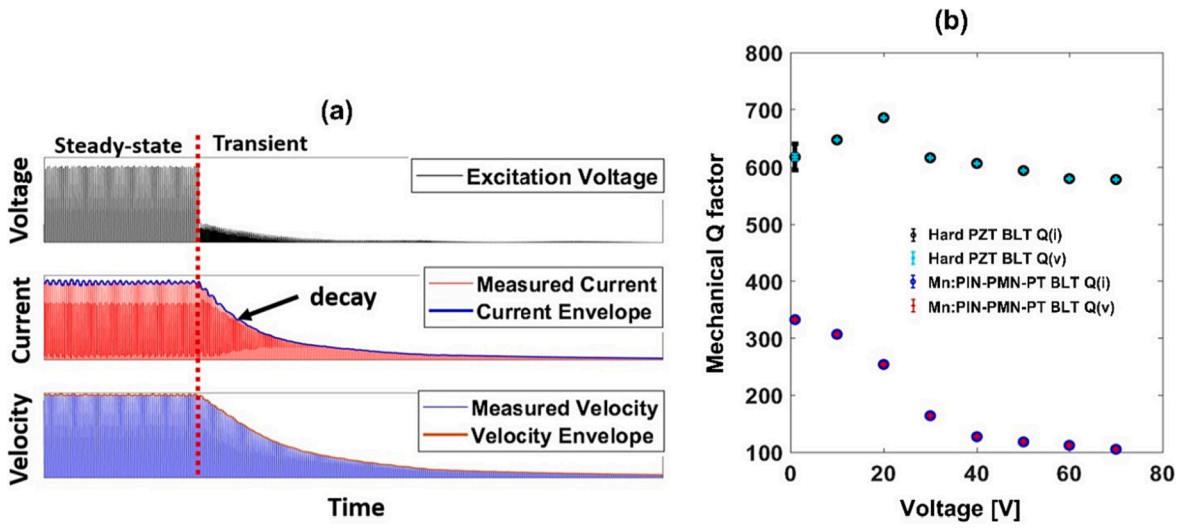

Fig. 11. (a) Voltage, current, and velocity time traces, including waveform envelopes acquired for transient decay measurements, to determine Q, (b) Q calculated for the two BLTs at increasing increments of voltage of the burst signal.

in BLTs is excitation level dependent and that, for a BLT incorporating Mn:PIN-PMN-PT, there are high losses at the excitation levels typical of power ultrasonic transducer operating conditions. This large reduction in Q risks negating the beneficial properties of Mn:PIN-PMN-PT.

4. Tissue cutting experimental setup

4.1. Tissue cutting test platform

The two ultrasonic surgical cutting devices were evaluated in cutting tests using the experimental platform shown in Fig. 12. Each ultrasonic surgical device is fixed onto the crossbeams via a force sensor (Kistler 9321b, Switzerland) to measure the cutting force. A linear actuator driven by a stepper motor (GLA750-STEP-20–3-285–390, Gimson Robotics, UK) with a stroke length of 285 mm is mounted between the table and the crossbeams to drive the ultrasonic surgical tool into the tissue mimic material which is clamped in a vice directly underneath the blade. An ultrasonic driving system (PDUS210 FLEX, Piezodrive, Australia) incorporating resonance tracking is used to maintain the displacement amplitude of the blade during cutting. To monitor the cutting temperature, a thermal camera (Micro-Epsilon TIM 160, Germany) is mounted close to the cutting site, focusing on the tip of the blade. A motion control system is used to drive the ultrasonic surgical tool at a constant velocity (feed rate). The crossbeams move in a vertical direction with the support of four linear rails and four embedded needle bearings to minimise lateral motion of the cutting device. This decoupled arrangement of linear actuator and ultrasonic device ensures friction between the bearings and shafts is not detected by the force sensor.

4.2. Electrical impedance matching network

For the ultrasonic cutting experiments, the same transformer setting in the Piezodrive system was used for both ultrasonic surgical devices. The output impedance of the transformer was then matched to the impedance of the surgical device, noting that the impedance magnitude of the Mn:PIN-PMN-PT device is almost nine times smaller than that of the hard PZT device (Table 2).

To aid the design of an electrical impedance matching circuit, the hard PZT device was modelled as an electrical circuit at resonance using the Butterworth Van Dyke (BVD) model [31] shown in Fig. 13 (a) where R_{SE} represents the radiation and mechanical losses of the transducer, C_{SE} represents the motion capacitance and L_{SE} represents the inductance to model the resonance of the ultrasonic surgical device and C_0 is the clamping capacitance. The simplest method to match a high load

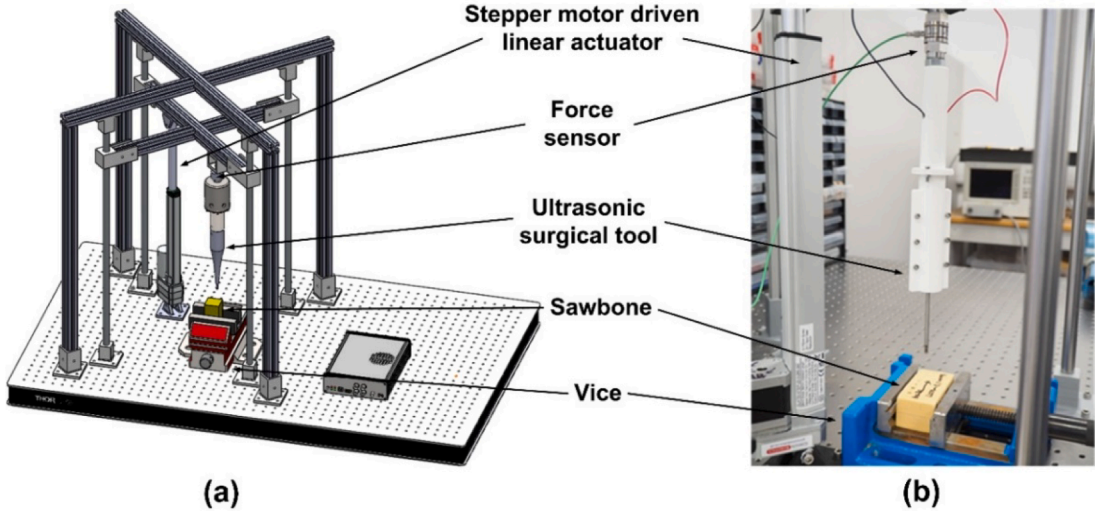

Fig. 12. Tissue cutting test rig showing the components of the system: (a) CAD model, (b) experimental rig.

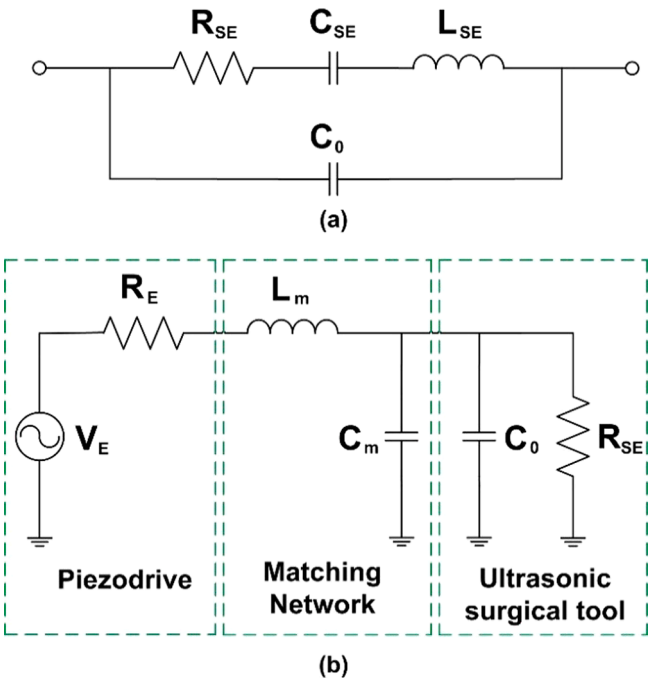

Fig. 13. Electrical impedance matching circuit: (a) BVD model representation at resonance, (b) simplified equivalent circuit at resonance with an L-C matching circuit.

impedance to a low source output impedance is to connect an inductor in series between the Piezodrive and the device and a capacitor in parallel with the device in an L-C matching network, Fig. 13(b). In resonance, the Langevin-style ultrasonic surgical device exhibits a purely resistive characteristic, therefore cancelling C_{SE} and L_{SE}. V_E represents the Piezodrive output, R_E is the resistance of its transformer and L_m and C_m are the inductance and capacitance of the L-C matching network respectively, with values calculated from Eq. (13) [31],

$$L_m = \frac{R_E}{\omega}\sqrt{\left(\frac{R_E}{R_{SE}} - 1\right)}$$
$$C_m = \frac{1}{\omega R_{SE}}\sqrt{\left(\frac{R_E}{R_{SE}} - 1\right)} - C_0 \quad (13)$$

where ω is the angular frequency of the ultrasonic device, and R_{SE}, C_{SE}, L_{SE} and C_0 are estimated and extracted from the small signal impedance measurement.

4.3. Cutting experiments

Two different materials were used in the cutting experiments, namely bone mimic (20 PCF solid foam blocks, Sawbone, USA) and chicken femur; the former presents a sample with consistent material properties, low strength and porosity that is often adopted as a simplified isotropic substitute for trabecular bone, and the latter presents a more realistic bone cutting set-up and a much higher strength sample that allows for the challenges of cutting cortical bone, albeit relying on freshly procured *ex-vivo* bone. The properties of the two specimen materials are presented in Table 3 [32,33,34].

Table 3
Cutting test sample material properties.

Material	20 PCF Sawbone	Chicken femur
Density [kg/m^3]	320	200
Compressive strength [MPa]	8.4	106.8
Poisson's ratio	0.30	0.30

5. Results and discussion

5.1. Displacement amplitude of the blade

The PDUS210-600 transformer of the Piezodrive was selected for the Mn:PIN-PMN-PT device as it has a measured impedance magnitude of 148.3 Ω (Table 3) that increases under load; this transformer has an optimal load impedance $R_E = 225$ Ω, with a working range of 146 Ω – 472 Ω. To match the optimal load impedance of the transformer for the hard PZT device, an L-C matching circuit was implemented, based on estimated parameters from the measured impedance of the device: $R_{SE} = 1291.1$ Ω, $L_{SE} = 21.24$ H, $C_{SE} = 2.82$ pF, and $C_0 = 726.35$ pF. Hence, the calculated matching inductance and capacitance (from Eq. (13)) are: $L_m = 3.8$ mH and $C_m = 12.32$ nF.

Fig. 14(a) shows the comparison of the impedance–frequency characteristics of the matched hard PZT and Mn:PIN-PMN-PT surgical devices. Both are now close to the optimal load impedance of the transformer ($R_E = 225$ Ω). Following the current control strategy of the Piezodrive, current was increased in increments of 0.05 A, from 0.05 to 0.2 A, and the peak-to-peak displacement amplitude at the tip of the blade was measured using a 1D laser Doppler vibrometer, Fig. 14(b). Both devices exhibit a linear displacement trend with increasing current, achieving close to 65 μm at 0.2 A. The displacement amplitudes are a close match, confirming the efficacy of the matching circuit in achieving a comparable efficiency for both devices driven using the same Piezodrive transformer.

5.2. Measured cutting force, cutting temperature, impedance and power

During tissue cutting experiments, the cutting force, cutting temperature, electrical impedance, and ultrasonic power were measured. The target depth of cut was 2.5 mm, making sure the round shape blade tip was fully engaged with the sample. A 60 μm peak-to-peak displacement amplitude of the blade was selected for both devices. For the Sawbone samples, experiments were conducted for four different cutting speeds, namely 0.025, 0.05, 0.075, and 0.1 mm/s. Only two cutting speeds, of 0.01 and 0.025 mm/s, were chosen for the chicken femur cutting experiments because the blades wear during bone cutting which reduces the validity of comparison.

5.2.1. Sawbone

From Fig. 15, the cutting force for all cutting speeds for both ultrasonic surgical devices is less than 2.5 N, with the hard PZT device exhibiting a lower cutting force. Cutting force increases with cutting speed but the highest two speeds result in very similar cutting forces for both devices. A cutting temperature of around 140 °C was measured for both devices and for all cutting speeds, the heating rate generally being higher for higher speeds, consistent with the friction developed between the blade and sample material.

Fig. 16 shows how the impedance magnitude increases under load as the blade progresses deeper into the sample. However, compared to the matched hard PZT surgical tool, the Mn:PIN-PMN-PT surgical tool presents a smaller increase in impedance magnitude, indicating greater stability. The ultrasonic power of both devices is largely stable but is higher for the Mn:PIN-PMN-PT device. Resonance frequency tends to increase slightly under load, apart from at the slowest cutting speed, with the change being slightly less for the Mn:PIN-PMN-PT device. In general, the results for this low strength bone mimic material show that both devices cut effectively, the hard PZT device cutting with a lower force and the Mn:PIN-PMN-PT device cutting with a more stable impedance under load.

5.2.2. Ex-vivo chicken femur

More significant differences in cutting performance between the two

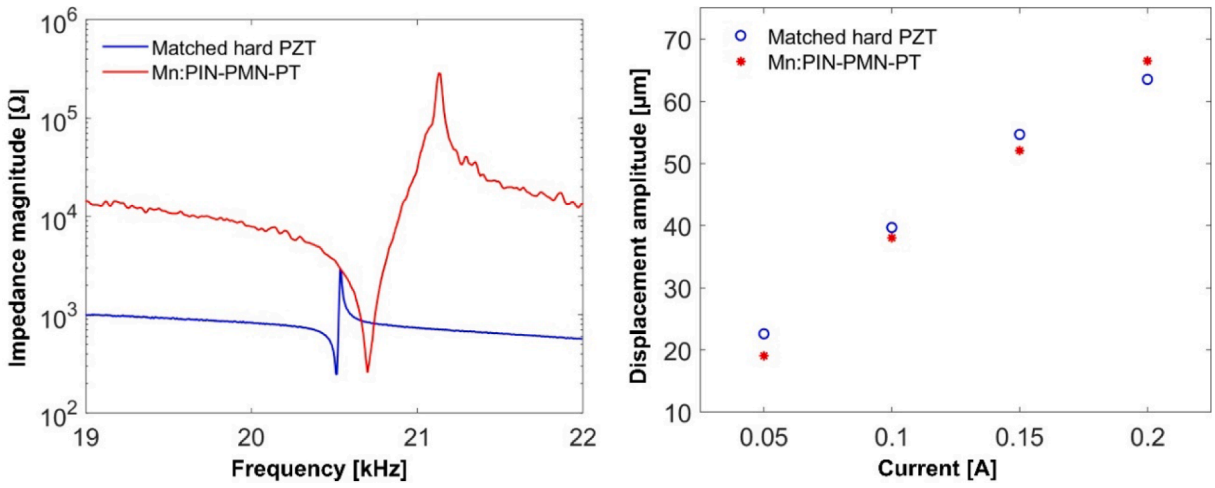

Fig. 14. (a) Impedance-frequency characteristics of the matched hard PZT and Mn:PIN-PMN-PT surgical devices. (b) Measured displacement amplitude of the two cutting blades as a function of current.

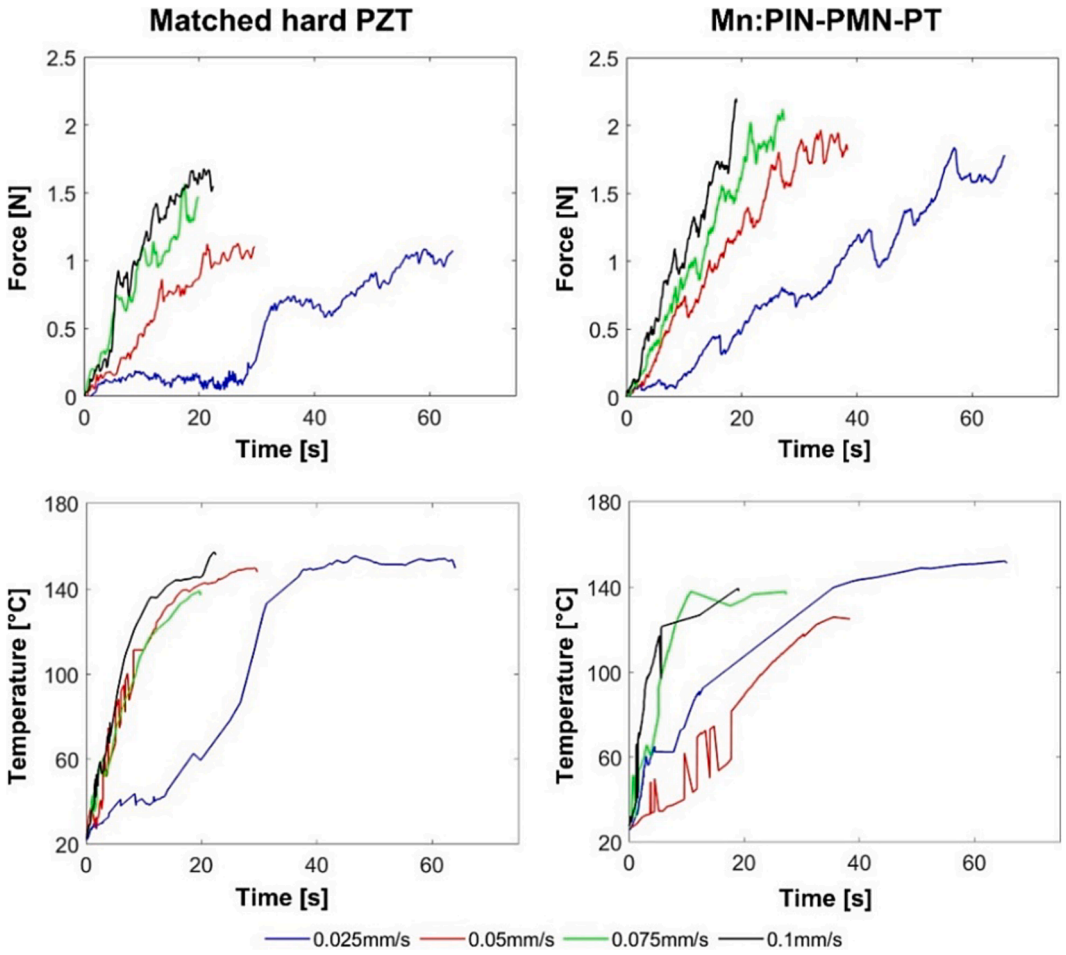

Fig. 15. Cutting force and temperature of the ultrasonic surgical devices cutting Sawbone samples at cutting speeds of 0.025, 0.05, 0.075, and 0.1 mm/s, with blade displacement amplitude 60 $\mu m_{p\text{-}p}$.

devices were found in cutting the *ex-vivo* chicken femur due to its significantly higher strength (more than ten times higher, see Table 3). The cutting force of the hard PZT device exhibits a sudden increase (Fig. 17), indicating that the cutting blade has stalled, and no cutting progress is being made. The temperature remains comparatively low since there is no further friction between the blade and bone. This failure to progress is also observed in Fig. 18 as a sudden increase in impedance and loss of resonance tracking capability. In comparison, the Mn:PIN-PMN-PT device is able to penetrate consistently more than 50 % deeper into the bone sample than the hard PZT device (Fig. 19). It also draws more power as the penetration depth increases, from 5 W to a maximal 15 W for the 0.025 mm/s feed rate, which is more than four

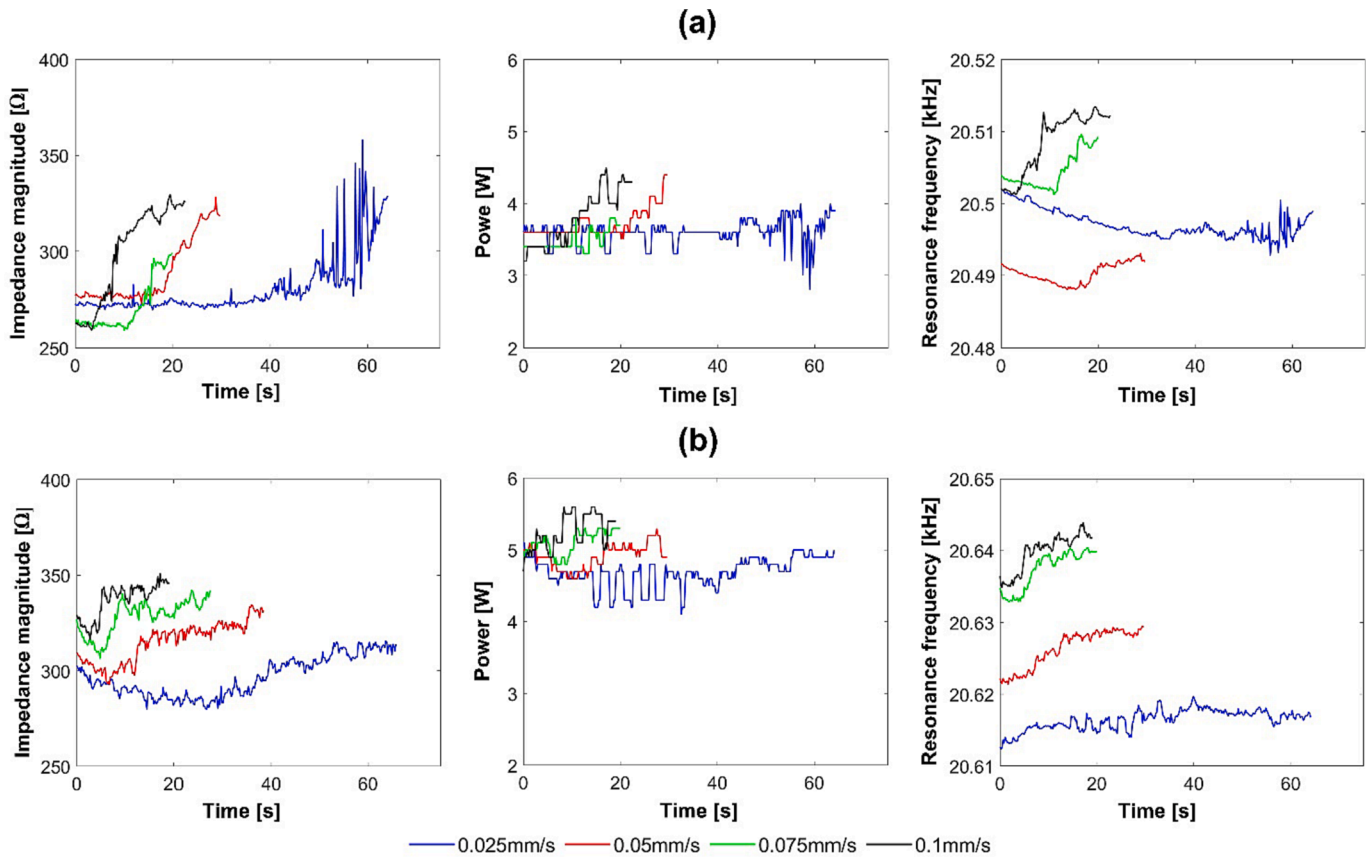

Fig. 16. Impedance magnitude, ultrasonic power, and change in resonance frequency of the (a) matched hard PZT and (b) Mn:PIN-PMN-PT surgical devices cutting into Sawbone at cutting speeds of 0.025, 0.05, 0.075, and 0.1 mm/s, with blade displacement amplitude 60 $\mu m_{P\text{-}P}$.

times higher than for the hard PZT device, despite the increase in the impedance magnitude. This is due to the significantly larger piezoelectric charge coefficient in the thickness direction, d_{33}, and hence the higher FoM and power density (see Table 1). The higher d_{33} leads to a lower impedance device and so there was no requirement for impedance matching. The impedance matching circuit used with the PZT device is tuned for no-load conditions and does not respond dynamically to changing load. Therefore, it is possible that the efficiency of the PZT device is worse under the much higher loads of cutting chicken bone than for cutting Sawbone. It can also be seen that the resonance frequency of the Mn:PIN-PMN-PT device remains stable throughout the cutting test.

The images in Fig. 19 show that the hard PZT device has not penetrated through the cortical bone whereas the Mn:PIN-PMN-PT device has done so successfully, making the blood in the trabecular bone visible. Overall, the results demonstrate that, for the same displacement amplitude of the cutting blade, the better load handling capability of the Mn:PIN-PMN-PT device meant it cut deeper into this higher strength sample.

6. Conclusions

A comparative study of Mn:PIN-PMN-PT piezocrystal material and hard PZT has been presented to determine the potential of incorporating Mn:PIN-PMN-PT in a transducer for power ultrasonics applications. Mn:PIN-PMN-PT rings were characterized and the full elasto-piezo-dielectric matrix reported in this study will facilitate future transducer designs. The material properties indicate that this piezocrystal has the potential to improve the performance and operational bandwidth of bolted Langevin transducers (BLTs).

Two half wavelength BLTs and two full wavelength ultrasonic surgical devices were tuned at 20 kHz to compare the performance of nominally identical devices incorporating Mn:PIN-PMN-PT and hard PZT. Despite the higher figure of merit of Mn:PIN-PMN-PT, no significant improvement was observed in the longitudinal vibration amplitude, although the bandwidth was significantly greater. This discrepancy between estimated and measured performance is attributed to the larger radial and axial elastic losses of the Mn:PIN-PMN-PT ring. The high cyclic deformation of the Mn:PIN-PMN-PT stack (see Fig. 8) means that the rings are deforming significantly more than the metal front and back masses causing energy losses at the interfaces between the rings and metal. PZT, on the other hand, does not exhibit this large deformation miss-match between the rings and the metal masses. These losses are supported by the measurements of Q shown in Fig. 11, where there is a much larger drop in Q at increasing excitation voltage, and therefore deformation, of the Mn:PIN-PMN-PT rings.

The nonlinear characterisation of Mn:PIN-PMN-PT piezocrystal rings in a standard BLT in both transient and steady-state conditions under high excitation levels has been described. Nonlinear effects, including frequency shifts, are more pronounced in the Mn:PIN-PMN-PT BLT than the hard PZT BLT, suggesting higher piezoelectric losses. This was also confirmed by evaluation of the effect of excitation level on Q, which showed a much larger reduction for devices incorporating Mn:PIN-PMN-PT.

In tissue cutting experiments, a half-wavelength cutting blade was attached to each BLT to create two surgical devices so that the two piezoelectric materials could be compared in a realistic power ultrasonic application. An L-C electrical impedance matching circuit was implemented to maximise the efficiency of energy transfer from the driving system to the ultrasonic surgical device, ensuring a valid comparison of the two devices. Cutting tests were conducted using a bone mimic and *ex-vivo* chicken femur. Results showed that both ultrasonic surgical

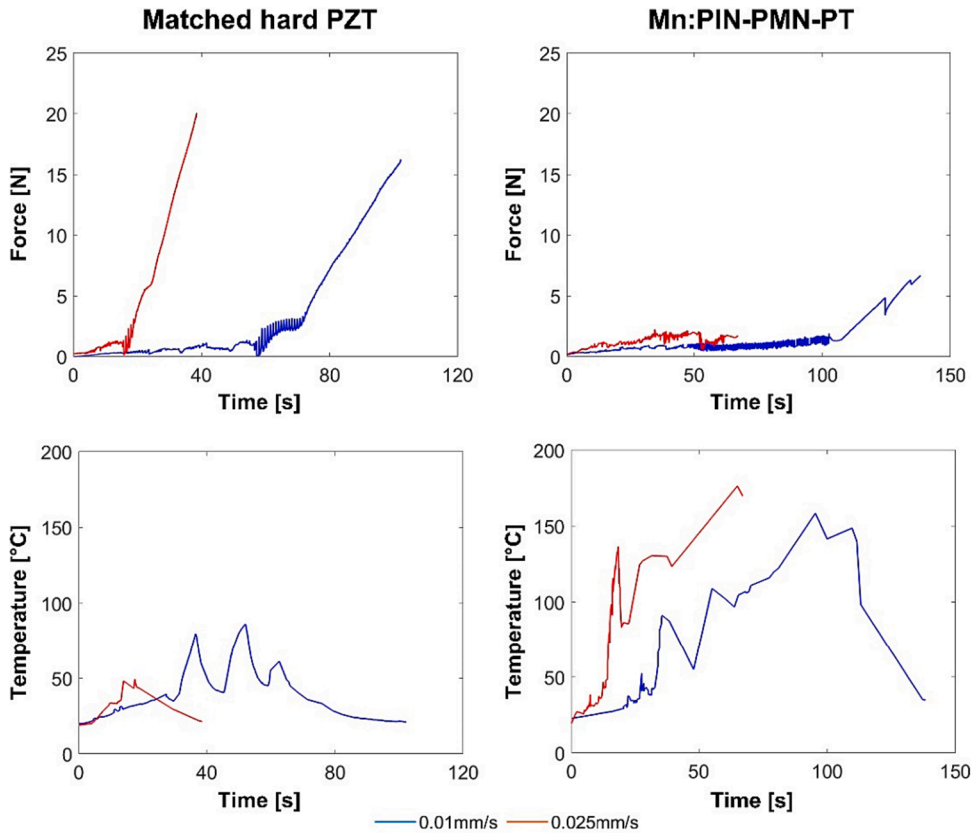

Fig. 17. Cutting force and temperature in cutting experiments on *ex-vivo* chicken femur.

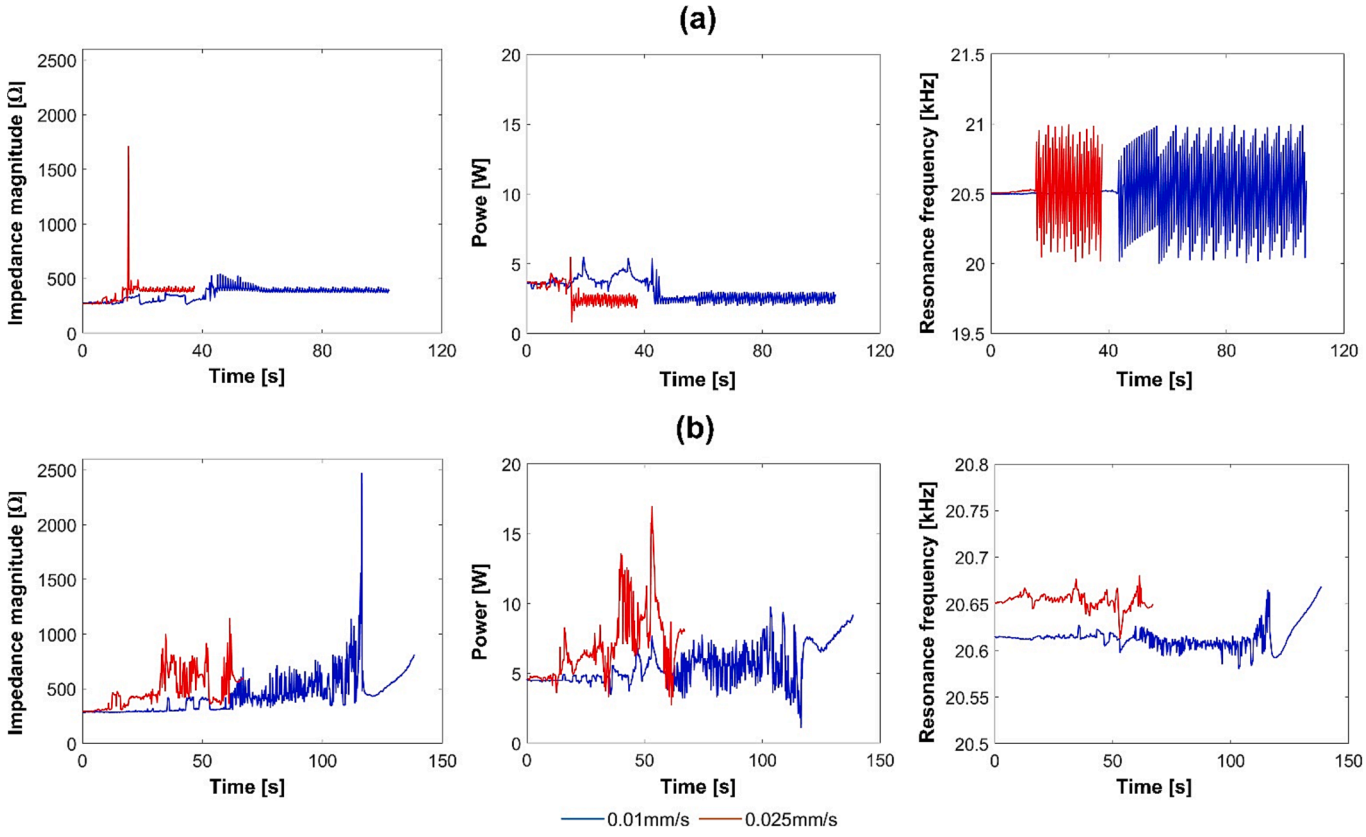

Fig. 18. Impedance magnitude, ultrasonic power, and resonance frequency of the (a) matched hard PZT and (b) Mn:PIN-PMN-PT surgical devices cutting into *ex-vivo* chicken femur.

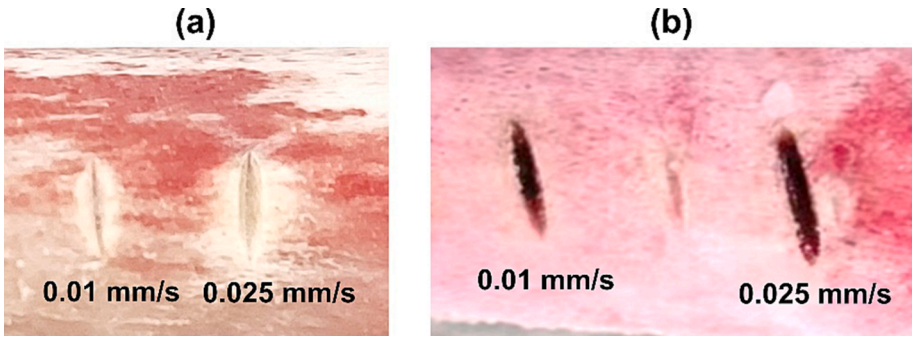

Fig. 19. *Ex-vivo* chicken femur samples showing the cuts made for the (a) matched hard PZT and (b) Mn:PIN-PMN-PT surgical devices operating at a displacement amplitude of 60 $\mu m_{p\text{-}p}$.

devices demonstrate similar and effective penetration of the low strength bone mimic, with low cutting force, relatively stable impedance and power consumption and little change in resonance frequency. However, for cutting tests in the much higher strength chicken femur, the Mn:PIN-PMN-PT surgical device achieved greater cutting depth for the same blade displacement amplitude, with low cutting force.

Despite the advantages confirmed for Mn:PIN-PMN-PT in a power ultrasonic BLT and cutting device, there are concerns due to the high losses and the much higher radial deformation of the transducer piezoelectric stack. Additionally, the presence of a phase transition at a relatively low temperature, T_{RT}, in Mn:PIN-PMN-PT piezocrystal could necessitate cooling in higher temperature applications. There may be other transducer configurations beyond the BLT which could benefit from the piezocrystal's properties, for instance exploiting other vibration modes, such as d_{31}, d_{32} and d_{36}, presents ripe possibilities for future study.

CRediT authorship contribution statement

Xuan Li: Conceptualization, Data curation, Formal analysis, Investigation, Methodology, Software, Validation, Visualization, Writing – original draft, Writing – review & editing, Project administration. **Nicola Giuseppe Fenu:** . **Nathan Giles-Donovan:** Formal analysis, Investigation, Validation, Data curation, Software. **Sandy Cochran:** Conceptualization, Funding acquisition, Project administration, Supervision, Writing – review & editing, Resources. **Margaret Lucas:** Funding acquisition, Project administration, Resources, Supervision, Writing – original draft, Writing – review & editing.

Declaration of competing interest

The authors declare that they have no known competing financial interests or personal relationships that could have appeared to influence the work reported in this paper.

Data availability

Data will be made available on request.

Acknowledgments

This work was supported by the EPSRC Programme, Ultrasurge – Surgery Enabled by Ultrasonics, EP/R045291/1. The authors thank TRS Technologies for providing the Mn:PIN-PMN-PT piezocrystal materials.

References

[1] S. Zhang, F. Li, X. Jiang, J. Kim, J. Luo, X. Geng, Advantages and challenges of relaxor-$PbTiO_3$ ferroelectric crystals for electroacoustic transducers - A review, Prog. Mater Sci. 68 (2015) 1–66.
[2] S. Zhang, T.R. Shrout, Relaxor-PT single crystals: observations and developments, IEEE Trans. Ultrason. Ferroelectr. Freq. Control 57 (10) (2010) 2138–2146.
[3] L. Zheng, R. Sahul, S. Zhang, W. Jiang, S. Li, W. Cao, Orientation dependence of piezoelectric properties and mechanical quality factors of $0.27Pb(In_{1/2}Nb_{1/2})O_3$–$0.46Pb(Mg_{1/3}Nb_{2/3})O_3$–$0.27PbTiO_3$: Mn single crystals, J. Appl. Phys. 114 (104105) (2013) 1–6.
[4] A.H. Chibli, M. Lucas, A. Gachagan, S. Cochran, Comparing Generation III Relaxor-PT Single Crystal with Modified PZT-4 for Power Ultrasonics Devices, IEEE International Symposium on Application of Ferroelectrics, Ohio USA, 2023.
[5] F. Bejarano, A. Feeney, R. Wallace, H. Simpson, M. Lucas, An ultrasonic orthopaedic surgical device based on a cymbal transducer, Ultrasonics 72 (2016) 24–33.
[6] M. Hofmann, A. Haeberlin, S. de Brot, A. Stahel, H. Keppner, J. Burger, Development and evaluation of a titanium-based planar ultrasonic scalpel for precision surgery, Ultrasonics 130 (2023) 1–14.
[7] K. Uchino, The development of piezoelectric materials and the new perspective, in *Advanced Piezoelectric Materials,* 2nd Edition, Chapter 1, pp. 1–92, 2017.
[8] L. Pardo, Piezoelectric ceramic materials for power ultrasonic transducers, *Power Ultrasonics*, *Applications of High Intensity Ultrasound*, Chapter 5 (2015) 101–125.
[9] IRE standards on piezoelectric crystals : determination of the elastic, piezoelectric, and dielectric constants - the electromechanical coupling factor, *IEEE Proceedings of the IRE*, pp. 764–778, 1958.
[10] A.A.N. Standard, IEEE standard on piezoelectricity, IEEE Transactions on Sonics and Ultrasonics 31 (2) (1984) 8–10.
[11] N. Giles-Donovan, N.G. Fenu, C. Stock, S. Zhang, S. Cochran, A Measure of energy density to quantify progress in Pb-free piezoelectric material development, IEEE International Ultrasonics Symposium, 2021, pp. 1–4.
[12] A. Mathieson, A. Cardoni, N. Cerisola, M. Lucas, Understanding nonlinear vibration behaviours in high-power ultrasonic surgical devices, Proceedings of the Royal Society a: Mathematical, Physical and Engineering Sciences 471 (2015) 1–19.
[13] X. Li, T. Stritch, K. Manley, M. Lucas, Limits and opportunities for miniaturizing ultrasonic surgical devices based on a Langevin transducer, IEEE Trans. Ultrason. Ferroelectr. Freq. Control 68 (7) (2021) 2543–2553.
[14] A. Mathieson, A. Cardoni, N. Cerisola, M. Lucas, The influence of piezoceramic stack location on nonlinear behavior of Langevin transducers, IEEE Trans. Ultrason. Ferroelectr. Freq. Control 60 (6) (2013) 1126–1133.
[15] E. Akça, H. Yılmaz, Lead-free potassium sodium niobate piezoceramics for high-power ultrasonic cutting application: modelling and prototyping, Process. Appl. Ceram. 13 (1) (2019) 65–78.
[16] N.G. Fenu, N. Giles-Donovan, M.R. Sadiq, S. Cochran, Full set of material properties of Lead-Free PIC 700 for transducer designers, IEEE Trans. Ultrason. Ferroelectr. Freq. Control 68 (5) (2021) 1797–1807.
[17] S. Li, L. Zheng, W. Jiang, R. Sahul, V. Gopalan, and W. Cao, Characterization of full set material constants of piezoelectric materials based on ultrasonic method and inverse impedance spectroscopy using only one sample, *Journal of Applied Physics*, vol. 114, no. 10, pp. 1–7, 2013.
[18] H. Jae Lee, S. Zhang, R.J. Meyer, N.P. Sherlock, T.R. Shrout, Characterization of piezoelectric ceramics and 1–3 composites for high power transducers, Appl. Phys. Lett. 101 (3) (2012).
[19] X. Li, N.G. Fenu, S. Cochran, M. Lucas, Comparison of performance of ultrasonic surgical cutting devices incorporating PZT piezoceramic and Mn:PIN-PMN-PT piezocrystal, IEEE International Ultrasonics Symposium (2021) 1–4.
[20] C.H. Choi, I.T. Seo, D. Song, M.S. Jang, B.Y. Kim, S. Nahm, T.H. Sung, H.C. Song, Relation between piezoelectric properties of ceramics and output power density of energy harvester, J. Eur. Ceram. Soc. 33 (7) (2013) 1343–1347.
[21] J. Kim, J. Lee, Parametric study of bolt clamping effect on resonance characteristics of Langevin transducers with lumped circuit models, Sensors 20 (7) (2020) 1–9.
[22] D.A. DeAngelis, G.W. Schulze, K.S. Wong, Optimizing piezoelectric stack preload bolts in ultrasonic transducers, Phys. Procedia 63 (2015) 11–20.
[23] A. Caronti, R. Carotenuto, M. Pappalardo, Electromechanical coupling factor of capacitive micromachined ultrasonic transducers, J. Acoust. Soc. Am. 113 (1) (2003) 279–288.
[24] T. Hemsel, E.G. Lierke, W. Littmann, T. Morita, Various Aspects of the Placement of a Piezoelectric Material in Composite Actuators, Motors, and Transducers, J. Korean Phy. Soc. 57 (4(1)) (2010) 933–937.

[25] A. Puškár, Cyclic stress-strain curves and internal friction of steel at ultrasonic frequencies, Ultrasonics 20 (3) (1982) 118–122.
[26] C. Campos-Pozuelo, J.A. Gallego-Juárez, Limiting strain of metals subjected to high-intensity ultrasound, ACTA Acustica 82 (6) (1996) 823–828.
[27] M. Umeda, K. Nakamura, S. Ueha, Effects of vibration stress and temperature on the characteristics of piezoelectric ceramics under high vibration amplitude levels measured by electrical transient responses, Jpn. J. Appl. Phys. Part 1 38 (9B) (1999) 5581–5585.
[28] A. Albareda, R. Pérez, J.A. Casals, J.E. García, D.A. Ochoa, Optimization of elastic nonlinear behavior measurements of ceramic piezoelectric resonators with burst excitation, IEEE Trans. Ultrason. Ferroelectr. Freq. Control 54 (10) (2007) 2175–2188.
[29] S. Mojrzisch, J. Twiefel, Phase-controlled frequency response measurement of a piezoelectric ring at high vibration amplitude, Arch. Appl. Mech. 86 (2016) 1763–1769.
[30] K. Nakamura, Evaluation methods for materials for power ultrasonic applications, Jpn. J. Appl. Phys. 59 (2020) 1–12.
[31] M. Garcia-Rodriguez, J. Garcia-Alvarez, Y. Yañez, M.J. Garcia-Hernandez, J. Salazar, A. Turo, J.A. Chavez, Low cost matching network for ultrasonic transducers, Phys. Procedia 3 (1) (2010) 1025–1031.
[32] Biomechanical Catalog Sawbone. https://www.sawbones.com/media/assets/product/documents/Solid_Rigid_Polyurethane_Foam_Properties.pdf.
[33] K. Damaziak, A. Charuta, J. Niemiec, M.R. Tatara, W. Krupski, D. Gozdowski, B. Kruzinska, Femur and tibia development in meat-type chickens with different growth potential for 56 days of rearing period, Poult. Sci. 98 (12) (2019) 7063–7075.
[34] N.C. Rath, G.R. Huff, W.E. Huff, J.M. Balog, Factors regulating bone maturity and strength in poultry, Poult. Sci. (2000) 1024–1032.